Transport and evolution of a pollution plume from northern China: A satellite-based case study

Can Li,[1,2] Nickolay A. Krotkov,[2,3] Russell R. Dickerson,[1] Zhanqing Li,[1,4,5] Kai Yang,[2,3] and Mian Chin[2]

[1]   On 5 April 2005, during the East Asian Study of Tropospheric Aerosols: An International Regional Experiment (EAST-AIRE) aircraft campaign, heavy loadings of SO_2 (20 ppb near ground, $1-3$ ppb at $\sim$2 km altitude) and dust with aerosol optical depth of $\sim$1 were measured over Shenyang, an industrialized city $\sim$600 km NE of Beijing. In this study, Ozone Monitoring Instrument (OMI) and MODIS satellite sensors are employed to look into this air pollution episode at a regional scale and to track the transport and evolution of the plume from China to the NW Pacific on the following days. A method is proposed to combine in situ measurements and trajectory tracer modeling with satellite observations to quantify the change in the SO_2 mass during plume transport. We demonstrate that an air mass factor correction is needed for quantitative use of the OMI SO_2 data, to account for the effects of the viewing geometry, the SO_2 profile shape, and the aerosol/cloud interference on retrievals. The total SO_2 loading of the plume decreased from $\sim$1.1 $\times$ 10^{11} g on 5 April to $\sim$5.0 $\times$ 10^{10} g on 7 April. The overall, e-folding lifetime of SO_2 in this plume, empirically derived from the rate of SO_2 decay, was $\sim$2 days (range of $1-4$ days). SO_2 to sulfate conversion increased the aerosol optical depth by $\sim$0.1$-$0.4 near the center of the plume on 6 and 7 April, while the loss of primary dust particles reduced the aerosol loading of the plume by a similar amount. Simulations with a chemical transport model suggest similar loss of dust and formation of sulfate within the plume during transport. The method established in this study can be further developed and applied to study other episodes of pollution transport and their impact on weather and climate.

1. Introduction

[2]   China's air pollution issue, a byproduct of phenomenal economic growth in the past few decades, has raised attention in light of its potential impact on human health, weather and climate, and global atmospheric chemistry. It has been demonstrated that midlatitude wave cyclones can build up and vent pollution plumes over China in springtime [e.g., *Fuelberg et al.*, 2003; *C. Li et al.*, 2007; *Li*, 2008]. These plumes with high concentrations of pollutants are generally of synoptic (or regional) scale. Under favorable meteorological conditions, they can travel far downwind off the east coast of China, and potentially influence large areas [e.g., *Fairlie et al.*, 2007; *Jacob et al.*, 2003; *Jaffe et al.*, 1999, 2003a, 2003b]. SO_2-to-suflate conversion can supply cloud condensation nuclei and may greatly affect the aerosol-cloud system over the northern Pacific [*Zhang et al.*, 2007]. Convection and advection can dilute a plume, while dispersing it to impact a larger area. Several approaches have been taken to study the transport and evolution of pollution plumes, each has strengths and weaknesses. Eulerian [e.g., *Carmichael et al.*, 2003] and Lagrangian [e.g., *Stohl et al.*, 2003] models can simulate the change of pollutants from source regions to receptor areas. But models need to be validated against observations. By intercepting a plume a few times on its path, Lagrangian or semi-Lagrangian airborne experiments can sample the plume at different stages [e.g., *Methven et al.*, 2006; *Baumgardner et al.*, 2008], but so far only a few experiments have been conducted.

[3]   Over the past several years, great progress has been made in satellite remote sensing of pollutants in the troposphere [e.g., *Martin*, 2008]. Satellite measurements have been used to track dust transport [e.g., *Huang et al.*, 2008; *Husar et al.*, 2001], characterize the chemical signature of frontal systems [e.g., *Liu et al.*, 2006], monitor long-term

[1]Department of Atmospheric and Oceanic Science, University of Maryland, College Park, Maryland, USA.
[2]NASA Goddard Space Flight Center, Greenbelt, Maryland, USA.
[3]Goddard Earth Sciences and Technology Center, University of Maryland Baltimore County, Baltimore, Maryland, USA.
[4]Institute of Atmospheric Physics, Chinese Academy of Sciences, Beijing, China.
[5]Nanjing University of Information Science and Technology, Nanjing, China.

[e.g., *Richter et al.*, 2005] and short-term [e.g., *Wang et al.*, 2007] change in pollutant levels, evaluate emission inventories [e.g., *Akimoto et al.*, 2006], infer surface air quality [e.g., *Engel-Cox et al.*, 2004], and constrain chemical transport models [e.g., *Allen et al.*, 2004]. The spatial coverage (normally hundreds to thousands of kilometers) and temporal resolution (usually daily) of polar satellites make them useful tools for tracking the evolution of synoptic pollution plumes. With daily global coverage, finer resolution, and almost simultaneous observations of multiple pollutants, a series of satellite sensors in the "A-train" constellation provide unprecedented capacity in measuring air pollution from space [*Anderson et al.*, 2005]. Currently, A-train includes several satellites (Aqua, CloudSat, CALIPSO, PARASOL, and Aura) with both active (e.g., Cloud Profiling Radar (CPR) and the Cloud-Aerosol Lidar with Orthogonal Polarization (CALIOP)) and passive (e.g., CERES, MODIS, OMI, TES, POLDER) sensors, providing key measurements of aerosols, gases, and clouds from space. So far, however, only few studies have used satellite data to quantify the change of pollutant loadings of these pollution plumes on an *episodic* basis.

[4] In April 2005, during the first intensive field campaign of the U.S.-China joint research project EAST-AIRE (East Asian Study of Tropospheric Aerosols: An International Regional Experiment) [*Z. Li et al.*, 2007a], several research flights were conducted near Shenyang, an industrialized, populated city (population: ~6 million) in China's northeastern region, and about 600 km NE of Beijing. The flight on 5 April was made in the polluted atmosphere ahead of an approaching cold front; substantial pollution was observed not only in the planetary boundary layer (PBL), but also in the free troposphere (FT) [*Dickerson et al.*, 2007]. Forward trajectory analysis and satellite data [*Dickerson et al.*, 2007] suggest that this pollution plume, with elevated pollutant levels in the free troposphere (FT), would travel far downwind to the east. This provides an excellent test case for improved quantification of an episodic pollution event by synergistically combining in situ measurements, A-train observations, and model simulation, and helps us gain deeper insight into the transport and transformation of pollutants that no single approach would provide. Taking advantage of the A-train, we looked at the 5 April air pollution episode on the regional scale, and tracked the evolution of the pollution plume as it moved eastward over the next few days, where in situ measurements were unavailable.

2. Data and Models

[5] The Ozone Monitoring Instrument (OMI) onboard NASA's Earth Observing System (EOS) Aura satellite retrieves SO_2 column content using UV in the wavelength range of $311-315$ nm [*Krotkov et al.*, 2006, 2008]. The PBL OMI SO_2 product has been validated against aircraft measurements during the EAST-AIRE campaign, and could distinguish between polluted and background conditions over northern China on a daily basis [*Krotkov et al.*, 2008]. The noise of the PBL SO_2 product can be as high as ~1.5 DU (Dobson unit) at the instrument's instantaneous field of view (FOV, 13×24 km at nadir), but the noise decreases when SO_2 plume is elevated above PBL during long-range transport. For a given SO_2 profile the noise can be further reduced through temporal and spatial averaging.

The ~1.5 DU noise level also implies that using the PBL algorithm on OMI could not accurately retrieve a significant portion of the plume where the SO_2 loading can fall below the detection limit. Section 3 details the corrections made to the operational product in this case study. In section 4.2, we discuss an approach using trajectory modeling to help estimate the part of the plume not seen by the satellite, and compare the corrected and the operational SO_2 data.

[6] Aerosol optical depth (AOD) retrieved from the MODerate resolution Imaging Spectrometer (MODIS) instrument aboard NASA's EOS/Aqua satellite provides remotely sensed aerosol information for our study, with a resolution of 10×10 km. The MODIS AOD retrieval algorithm derives aerosol properties over dark surfaces (cloud, ice, snow, sun glint, and desert free), and is based on a "lookup table" approach; that is, the observed radiation field is compared against the precomputed radiative transfer calculations with a set of assumed aerosol and surface parameters [*Remer et al.*, 2005]. The best fit found through the comparison is the solution to the inversion. Over oceans, the MODIS algorithm assumes one fine and one coarse lognormal mode, if properly weighted, combine to represent ambient aerosol properties. Over land, the surface reflectance can be derived from longer wavelength MODIS channels, as atmospheric extinction due to aerosols is generally low in the 2.12 μm band. An earlier version of the MODIS land algorithm assumed constant ratios between the surface reflectance at 0.47 and 0.66 μm and at 2.12 μm. The recently updated (collection 5: C005-L) MODIS land algorithm [*Levy et al.*, 2007a, 2007b] parameterizes this spectral surface reflectance relationship as a function of viewing geometry and surface type (NDVI: normalized difference vegetation index). The algorithm also employs new aerosol models derived from surface Sun photometer measurements (AErosol RObotic NETwork: AERONET); and simultaneously retrieves surface reflectance, AOD, and fine mode aerosol weighting. The MODIS AOD product has been validated against measurements made by both automated Cimel Sun photometer at two stations [*Mi et al.*, 2007] and a network of handheld Sun photometers at 25 stations [*Z. Li et al.*, 2007b] over China, and the collection 5 data show much improved agreement with surface observation. Both Aura and Aqua satellites are part of the A-train satellite constellation and pass over the Shenyang region ~15 min apart at about 1330 local time (LT) (0530 UTC).

[7] The HYSPLIT model (R. R. Draxler and G. D. Rolph, HYSPLIT (HYbrid Single-Particle Lagrangian Integrated Trajectory) Model, 2003, access via NOAA ARL READY Web site htttp://www.arl.noaa.gov/ready/hysplit4.html) along with NCEP global reanalysis data are used to calculate forward trajectories in this study. Seventy-two hour forward trajectories from eight layers (every 500 m from 250 to 3750 m above ground level) are initiated from $0.5° \times 0.5°$ grid cells in the region of $35-49°$N, $117-134°$E (black rectangular boxes in Figure 2a in section 4.1), at 0500 UTC, 5 April 2005. Each trajectory represents an air parcel $0.5° \times 0.5° \times 500$ m in size, and is tagged with AOD and SO_2 retrieved by MODIS and OMI and weighted with aircraft profiles (aircraft-measured aerosol scattering and SO_2 concentration are integrated every 500 m and normalized to generate weighting profiles in this case). The size of the grid

cells is selected so that the OMI SO_2 data can be spatially averaged to reduce the noise, while some details of the plume distribution can still be retained. AOD retrievals are missing in some grid cells; and trajectories originating from these grid cells are labeled with the mean AOD of adjacent grid cells. Grid cells with SO_2 below a certain threshold value (see section 4.2) are considered "nondetectable" by OMI. Trajectories from these grid cells are assigned half of the threshold SO_2. There is no special treatment for parcels with relatively low AOD, as MODIS appears to have good sensitivity even for low aerosol loadings [*Levy et al.*, 2007a, 2007b]. Assuming that pollutants within each parcel are conserved, these "tagged" air parcels together can project and map the spatial distribution of SO_2 and AOD in the plume.

[8] This transport event was also examined with Goddard Chemistry Aerosol Radiation and Transport (GOCART) model simulations. Driven by the assimilated meteorological fields of the Goddard Earth Observing System Data Assimilation System (GEOS DAS), GOCART is a global model with a horizontal resolution of 2 (latitude) by 2.5 (longitude) degrees and 30 vertical layers in the version used in this study. The output of the GOCART model includes SO_2 as well as concentrations and aerosol optical depth of sea salt, sulfate, organic and elemental carbonaceous compounds, and dust [*Chin et al.*, 2000, 2002; *Ginoux et al.*, 2001].

3. Air Mass Factor Correction for the Operational OMI SO_2 Product

[9] In OMI retrievals, the retrieved slant column SO_2 density (SCD) is converted to total SO_2 vertical column density (VCD) with air mass factor (AMF), defined as the ratio between the slant column to the vertical column,

$$\text{total } SO_2 \text{ VCD} = \frac{\text{SCD}}{\text{AMF}}. \tag{1}$$

AMF is a function of SO_2 profile, surface albedo (R_s), viewing geometry (viewing angle: θ, solar zenith angle: θ_0, and relative solar azimuth angle: φ), total column ozone (Ω), aerosols, and clouds [*Krotkov et al.*, 2008],

$$\text{AMF} = \int_0^\infty m(z, R_s, \Omega, \theta, \theta_0, \phi) n_{SO_2}(z) dz \tag{2}$$

$$m(z) = \frac{\partial \ln(I_{TOA})}{\partial \tau_{SO_2}(z)}, \tag{3}$$

where $m(z, R_s, \Omega, \theta, \theta_0, \varphi)$ is the vertically resolved OMI SO_2 sensitivity, I_{TOA} is the OMI measured solar normalized radiance at TOA (top of the atmosphere), $\tau_{SO2}(z)$ is the SO_2 absorption optical thickness at the layer z (km), and $n_{SO2}(z)$ is normalized SO_2 vertical profile. In the operational OMI PBL SO_2 product, a constant AMF value of 0.36 is used. This operational AMF assumes cloud- and aerosol-free conditions, solar zenith angle of 30°, surface albedo of 0.05, surface pressure of 1013.13 hPa, midlatitude ozone profile of 325 DU, and a vertical SO_2 profile typically observed over the eastern U.S. in summer, with most of the SO_2 below 900 hPa [*Taubman et al.*, 2006].

[10] These assumptions may not be valid under some conditions, and AMF correction of the operational SO_2 data is needed. For example, OMI is more sensitive to SO_2 above the PBL; using the operational AMF assuming low plume height, the SO_2 loading in an elevated plume would be overestimated. Given gaseous and aerosol vertical profiles and optical properties the AMF can be obtained from a forward radiative transfer calculation; the corrected SO_2 column amount would be

$$SO_2(\text{corrected}) = \frac{0.36}{\text{AMF(corrected)}} SO_2(\text{operational}). \tag{4}$$

Radiative transfer calculation of AMF for each pixel or grid cell is so computationally demanding that it is impractical. *Krotkov et al.* [2008] show that the total ozone and viewing geometry corrections of AMF can be combined and parameterized through linear regression with respect to the slant column ozone (SCO),

$$\text{AMF(corrected)} = r_0 - r_1 \cdot \text{SCO} \tag{5}$$

$$\text{SCO} = \Omega \cdot (\sec(\theta) + \sec(\theta_0)), \tag{6}$$

where Ω is the total column ozone measured by OMI. The slope (r_1) and the intercept (r_0) of the linear regression depend on the normalized SO_2 vertical profile, surface albedo, relative solar azimuth angle, aerosols, and clouds. This linear regression could be further simplified, as R_s is normally small in the UV band for SO_2 retrieval (311–315 nm), its unaccounted variability causing an error less than 15%, and changes of φ would result in typically ±10%, and in extreme cases no more than 20% error in AMF. In this study, AMF-SCO regression coefficients are derived under various assumptions concerning SO_2 profile, aerosols, and clouds. For example, on a given day, the clear-sky AMF-SCO relationship is derived with normalized SO_2 and aerosol vertical profiles and the average MODIS AOD around the core part of the plume, for two different aerosol types (industrial and dust):

$$\text{AMF}_{C,INDU} = r_{0,C,INDU} - r_{1,C,INDU} \cdot \text{SCO} \tag{7}$$

$$\text{AMF}_{C,DUST} = r_{0,C,DUST} - r_{1,C,DUST} \cdot \text{SCO}, \tag{8}$$

where $\text{AMF}_{C,INDU}$ and $\text{AMF}_{C,DUST}$ stand for the corrected clear-sky AMF for industrial and dust aerosols, respectively. The retrieval assumes the same single scattering albedo (0.9) at 550 nm for both aerosol types, but each has a different size distribution and spectral dependence of absorption. $\text{AMF}_{C,INDU}$ and $\text{AMF}_{C,DUST}$ are then weighted with dust (AOD_{DUST}) and total AOD (AOD_T) to obtain the clear-sky AMF (AMF_C),

$$W = \frac{\text{AOD}_{DUST}}{\text{AOD}_T} \tag{9}$$

$$\text{AMF}_C = \left[(1 - W) \cdot r_{0,C,INDU} + W \cdot r_{0,C,DUST}\right] \\ - \left[(1 - W) \cdot r_{1,C,INDU} + W \cdot r_{1,C,DUST}\right] \cdot \text{SCO}. \tag{10}$$

For this particular case, as will be shown in sections 4 and 5, dust is the dominant aerosol species in the plume throughout the whole study period, and we assume W = 1 (all dust) in AMF calculations. Results of a sensitivity test using more accurate weight based on GOCART model output are given in section 5.

[11] The AMF under cloudy conditions can be calculated similarly for the same two aerosol types, using OMI measured Lambertian effective reflectivity (LER) at 331 nm [Ahmad et al., 2004] and MODIS retrieved cloud top pressure [Menzal et al., 2006]. We assume that high clouds are mostly thin and have little influence on SO$_2$ retrieval. Low clouds on the other hand enhance OMI sensitivity to SO$_2$ above them. As a first-order approximation in radiative transfer calculations for the two cloudy days (6 and 7 April), overcast conditions are assumed: a homogenous cloud "floor" with the mean reflectance of the region is placed at the average cloud top height of MODIS low clouds. The resulting AMFs are then combined using the weighting factor derived with equation (9) (W = 1 for this study). No correction was made for the mostly cloud-free sky conditions on 5 April.

[12] Vertical profiles of SO$_2$ and aerosols were obtained during the flight on 5 April over NE China (see section 4.1 for details), and are used for AMF correction for this day. The aerosol optical depth over the flight region on the day was measured from the surface using a handheld Sun photometer (measurement location: 41.5°N, 123.6°E). As will be discussed in section 4, the main body of the plume moved to northern Japan on 6 April and the NW Pacific on 7 April. To make AMF correction for the SO$_2$ profile shape, we calculate the trajectory-projected SO$_2$ loadings (see section 2) at different heights (every 500 m, 0−6500 m) over the center of the plume (40°N−45°N, 138°E−144°E on 6 April; 35°N−40°N, 160°E−165°E on 7 April) as the plume moved eastward. The resulting normalized vertical distributions of SO$_2$ are referred to as trajectory-projected profiles. They are similar to GOCART simulated SO$_2$ profiles (not shown) and are employed for the AMF calculations for 6 and 7 April, as aircraft measurements are unavailable on these days. On 6 April, a NIES (National Institute for Environmental Studies) lidar system [Shimizu et al., 2004] determined the aerosol vertical profile of the plume as it passed over Sapporo, Japan (43.1°N, 141.3°E). This lidar-measured aerosol profile is used for AMF calculation for the day. Similar to SO$_2$, aerosol profile projected with the forward trajectory model is used for AMF correction for 7 April.

[13] As a summary, the operational SO$_2$ product assumes fixed viewing geometry, fixed SO$_2$ plume height, and aerosol-cloud-free conditions. In this study the viewing geometry is corrected for by parameterization against the slant ozone column; the SO$_2$ plume height in the operational product is replaced with aircraft measurements and trajectory projections; the MODIS product provides information about clouds and aerosol loading for AMF calculation; aircraft measurements, lidar observation, and trajectory modeling supply information concerning aerosol vertical distribution. These corrections can improve the quality of OMI SO$_2$ data. In section 4.2 we compare the AMF-corrected and the operational SO$_2$ data.

4. Results

4.1. Transport and Evolution of the Plume

[14] The weather conditions and air quality measured by aircraft near Shenyang on 5 April, 2005 have been discussed by Dickerson et al. [2007], and are only briefly reviewed here. Weather during this prefrontal flight featured strong surface winds from the south, local dust emissions and low visibility (4−5 km). Winds veered with altitude and became westerly in the middle troposphere. The aircraft detected ∼20 ppb SO$_2$ within the PBL, and 1−3 ppb SO$_2$ in the FT, which translates into a vertical column amount of ∼2 DU. The vertical distribution of aerosols was similar to that of SO$_2$, with ∼500 Mm^{-1} (10^6 m^{-1}) scattering in the PBL and ∼100 Mm^{-1} scattering in the FT. The aircraft-integrated and surface observed AOD (550 nm) were comparable at ∼1.0. The Ångström Exponent (AE, 440/660 nm) from the surface AOD measurements was about 0.8, suggesting overall large aerosol particle size. The single scattering albedo at 470 nm retrieved for the day is 0.87 (K.-H. Lee, personal communication, 2007), indicating strongly light-absorbing aerosols.

[15] Satellite observations, in agreement with aircraft and surface measurements, detected high levels of SO$_2$ and aerosols on 5 April, but over a much larger area. The average OMI SO$_2$ column content in the region near Shenyang (rectangular box, Figure 1a) was about 1.5 DU, with some "hot spots" exceeding 3 DU. The mean AOD (550 nm) in the same region was ∼0.7, and higher values (∼1.8) were found to the southwest (Figure 2a). Fairly high OMI-observed Aerosol Index (AI, > 2, Figure 3d) in the region implied the existence of absorbing aerosols. Dust was likely the dominant aerosol compound according to the high AI (>2), the low AE (∼0.8), meteorological records (blowing dust observed at meteorological stations around the Shenyang region), and GOCART output (plot not shown, simulated dust AOD contributes ∼85% of the total AOD).

[16] As shown in Figures 1 and 2, trajectory calculations indicate that the pollution plume in general traveled eastward, reaching northern Japan on 6 April (plume peak height 1−1.5 km) and the NW Pacific on 7 April (plume peak height 1.5−2 km). As suggested by van Donkelaar et al. [2008], most SO$_x$ (SO$_2$ and sulfate) transported across the Pacific Ocean from East Asia is at 600−800 hPa. OMI and MODIS successfully captured the pollutants on both days, taking snapshots of the plume (Figures 1 and 2). The core part of the plume depicted by the OMI aerosol index (Figures 2e and 2f) resembles that mapped with trajectories (Figures 2h and 2i), suggesting that the forecast plume agrees with satellite observations and that AI could be a useful tool for tracking aerosol transport.

[17] The trajectory calculations use SO$_2$ and aerosols as inert tracers and therefore only account for the advection and dilution of the plume (Figures 1 and 2). OMI retrieved SO$_2$, on the other hand, reflects the combined effect of transport, chemical conversion, change in satellite sensitivity, and noise, as does the MODIS-retrieved AOD. Exam-
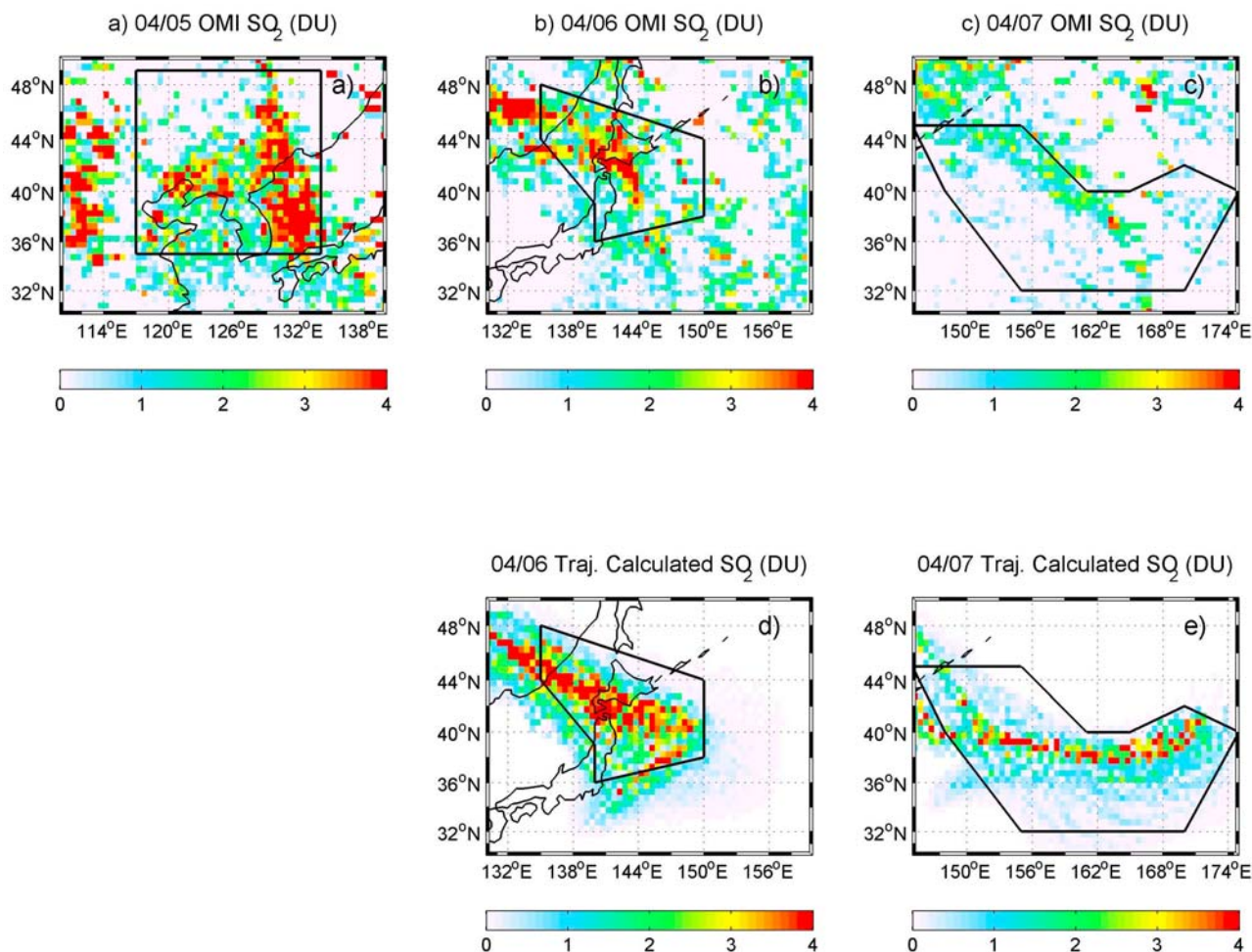
Figure 1. (a, b, and c) OMI-retrieved and (d and e) trajectory-calculated SO_2 from 5 to 7 April near the main part of the pollution plume. The rectangular box in Figure 1a indicates the area from which forward trajectories are initiated. Polygon boxes in Figures 1b and 1c are examples of the boxes used to represent the core part of the plume, and to calculate the total SO_2 mass on 6 and 7 April.

ining Figures 1 and 2 shows that near the major part of the plume, OMI SO_2 is considerably lower than trajectory SO_2 (e.g., Figure 1b versus Figure 1d), while MODIS AOD is greater than trajectory projection (e.g., Figure 2b versus 2h). This indicates that as the pollution plume moved downwind, SO_2, a precursor of sulfate aerosols, was lost whereas new sulfate aerosols were introduced (or the aerosol extinction was enhanced). Dust remained the dominant aerosol species throughout the three-day period, as evidenced by OMI AI (Figures 2d, 2e, and 2f) and GOCART model simulated AOD, but sulfate became increasingly important over time (section 5). It is possible that the satellite sensors detected signal of primary trace gas (SO_2) converting to secondary aerosols (sulfate). Next we discuss the evolution of the chemical properties of the plume.

4.2. Change in the Total Mass of SO_2: Comparison Between Operational and AMF-Corrected OMI SO_2 Data

[18] Clouds, satellite orbit, surface reflectance, and the signal-to-noise ratio are some restraining factors limiting observation of pollution plumes from space. During transport, chemical/physical losses reduce the concentration of SO_2, and dispersion dilutes it. For part of plume initially observed by OMI, the actual SO_2 column amount may drop to below the detection limit (but above zero) and this part is no longer seen by OMI, resulting in underestimation of the total SO_2 loading within the plume. On the other hand, during long-range transport some SO_2 may be lofted from near the surface to higher altitudes into the FT. As OMI is more sensitive to SO_2 at higher altitudes, assuming the same vertical distribution can lead to overestimation of the total SO_2. Low-level clouds may further enhance the OMI sensitivity to SO_2 above them, but can block the signal below them. In short, satellite sensors can picture the plume daily, but often only detect part of the plume. To correct for the undetected part of the plume, we define a dispersion weighting factor (DWF). Taking 6 April as an example, we first select a polygon box (P1) covering a good part of the plume with strong trajectory-projected SO_2 signal (e.g., the polygon box in Figure 1d). The DWF for this box (DWF_{P1}) is the ratio between trajectory-projected SO_2 mass within P1 ($M_{P1, TRAJ}$) and the initial total SO_2 of the plume (M_1), calculated from the OMI retrievals on 5 April (rectangular box, Figure 1a) and kept constant in trajectory calculations. Weighting the OMI-retrieved SO_2 mass within P1 ($M_{P1,SAT}$) with
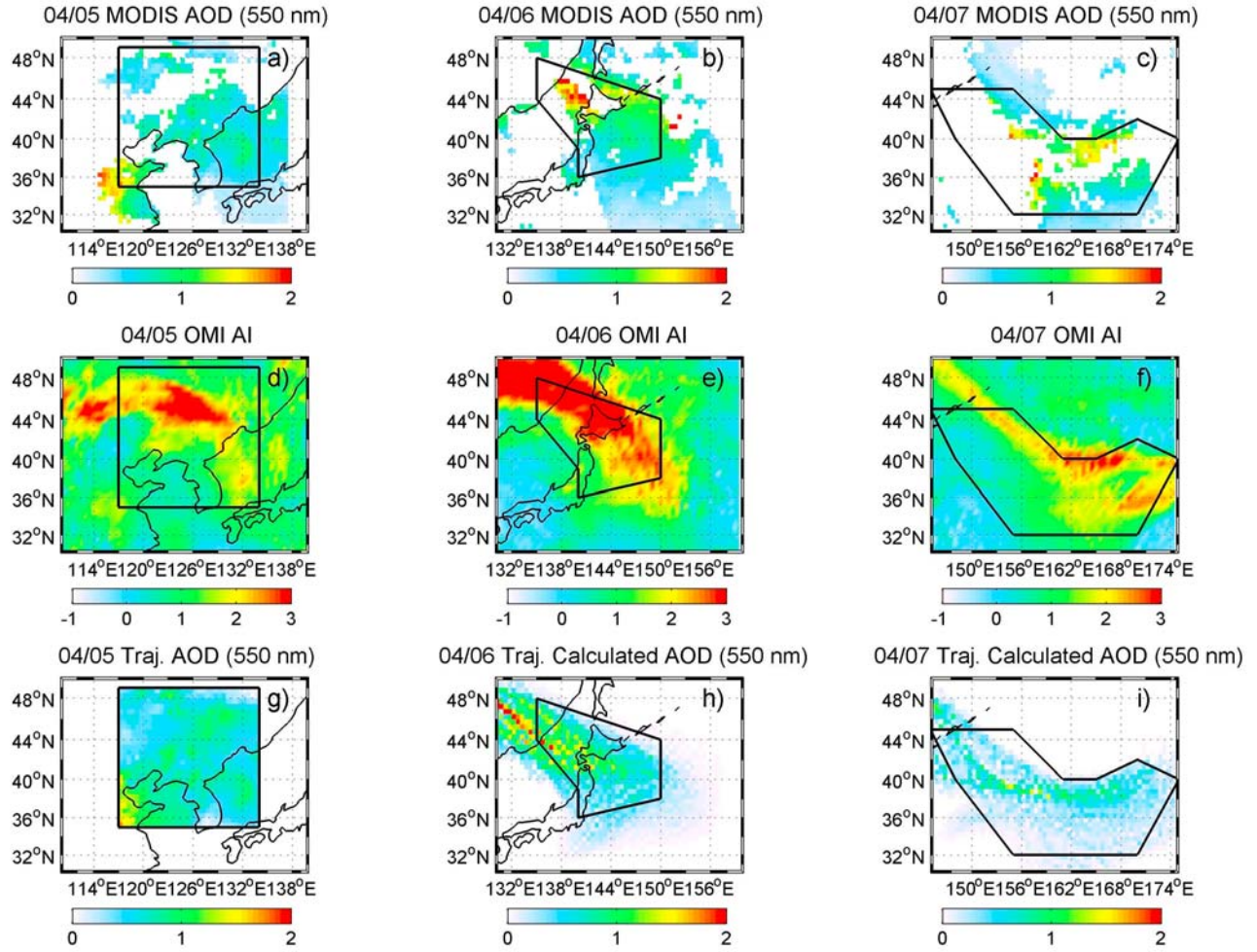
Figure 2. (a, b, and c) MODIS-retrieved AOD, (d, e, and f) OMI aerosol index (AI), and (g, h, and i) trajectory-projected AOD from 5 to 7 April 2005. Missing MODIS AOD retrievals in Figures 2a–2c are mainly due to clouds, Sun glint, or high surface reflectance (5 April). These grid cells are not included in the calculation of the average MODIS AOD.

DWF_{P1} gives an estimate of the total SO_2 mass on 6 April ($M_{2, P1}$):

$$M_{2,P1} = \frac{M_{P1,SAT}}{DWF_{P1}} \tag{11}$$

$$DWF_{P1} = \frac{M_{P1,TRAJ}}{M_1}. \tag{12}$$

The inherent assumption here is that the spatial distribution of column SO_2 projected by the trajectory tracer model is the same as the actual distribution with chemical/physical losses. To estimate the uncertainties introduced by the above method, five polygon boxes ($P1 \ldots P5$) of different size and shape are selected each day for 6 and 7 April (Figures 1 and 2 show one example for each day). Each polygon has a corresponding estimated total SO_2 mass (e.g., $M_{2,P1} \ldots M_{2, P5}$). The average is taken as the estimated total SO_2 mass, for example on 6 April,

$$M_2 = \sum_{i=1}^{5} M_{2,Pi}/5. \tag{13}$$

Assuming that there is a large difference between the tracer model–projected and the actual distributions of column SO_2, the SO_2 total mass calculated with different polygon boxes likely will be quite different. For 6 April, the biggest polygon box is a factor of 3 larger than the smallest box, yet the total SO_2 derived using the two boxes only differs by ∼10% (standard deviation about 5% of the mean from five boxes, Figure 3b). One might imagine that the difference between the tracer model–projected and the actual SO_2 distributions would grow with time, as uncertainty in trajectories becomes larger and more SO_2 is lost. This appears to be the case in this study: for 7 April, the biggest polygon box is 3.5 times as large as the smallest one, and the derived total SO_2 is different by ∼100% (standard deviation about 40% of the mean from five boxes, Figure 3b). From the above analysis, the uncertainty introduced by the assumption in equations (11) and (12) appears to be relatively small (about ±10%) for 6 April but grows fast to around ±80% for 7 April (not including uncertainties in OMI retrievals).

[19] Pixels or grid cells with retrieved SO_2 under a certain threshold (presumed detection limit) are considered undetectable by OMI, and are assumed, on average, to contain
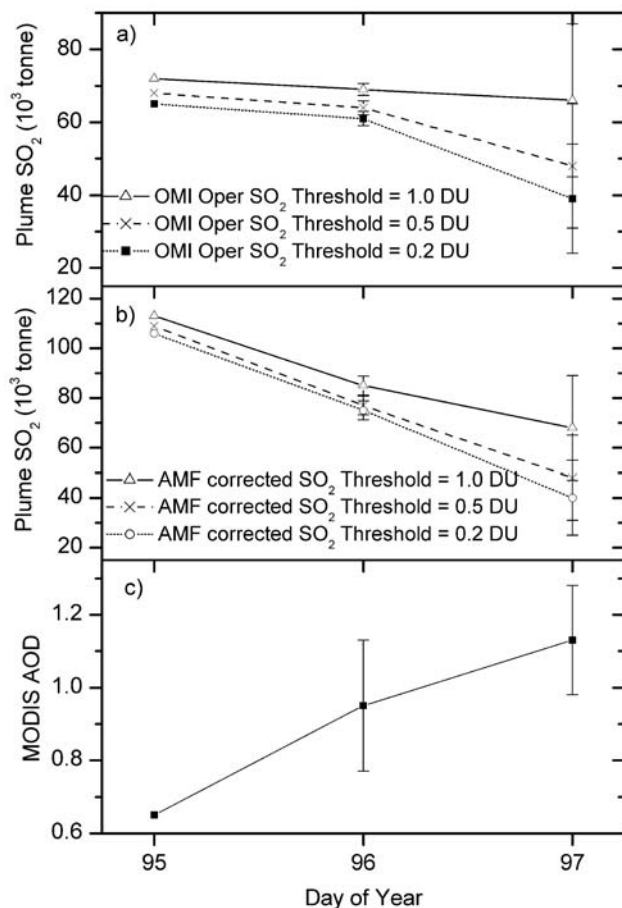
Figure 3. Total SO$_2$ mass of the plume calculated from the (a) operational and (b) AMF-corrected SO$_2$ data; (c) the average AOD near the main body of the plume (within polygon boxes in Figure 2). Error bars represent the standard deviation of estimates using different polygon boxes. Estimates of SO$_2$ mass with different assumptions diverge on 7 April, but diverge much less on 6 April. When calculating the total SO$_2$ mass, grids with SO$_2$ below threshold values are assumed to contain, on average, half of the threshold SO$_2$ and are included in the total mass calculation.

half of the threshold column SO$_2$. Three threshold values (0.2, 0.5 and 1.0 DU) are chosen to approximate the variety of factors that might influence the OMI sensitivity to SO$_2$. If for a polygon box the retrieved SO$_2$ of some grids is 0.2–0.5 DU, in SO$_2$ mass calculation using the 1.0 DU threshold, these grids will be assigned 0.5 DU of SO$_2$. The resulting SO$_2$ mass would be greater than that calculated using the 0.2 DU threshold (Figure 3a). For 6 April, the estimated total SO$_2$ using 0.2, 0.5, and 1.0 DU as threshold is 67, 69, and 74 kt, respectively. For 7 April, the estimates with these three threshold values stand at 34, 42, and 60 kt.

[20] Figure 3a shows the change of the total SO$_2$ mass loading of the plume from 5 to 7 April, estimated from the operational OMI SO$_2$ product using the method discussed above. In comparison, the time series of the SO$_2$ loading of the plume in Figure 3b are calculated with exactly the same method (the same polygon boxes and threshold values), but from the SO$_2$ data after the AMF correction described in section 3. With the interference of dust particles corrected

for, the SO$_2$ mass within the plume over the source region (35°N–49°N, 117°E–134°E) on 5 April increases by more than 50%, from ~70 kt (10^3 tonne or 10^6 g) to ~110 kt. The latter value represents roughly 0.05% of the annual global emissions [*Intergovernmental Panel on Climate Change*, 2001]. The SO$_2$ loading of the plume based on the operational product changes little from 5 to 6 April (Figure 3a). This is problematic as SO$_2$ normally has a lifetime of few days in the lower troposphere, and after one day a considerable drop in the total SO$_2$ mass within the plume is expected. The SO$_2$ loading on 6 April calculated with the AMF-corrected data is ~80 kt, ~30 kt less than on 5 April. Estimates for 7 April from both the operational SO$_2$ data (Figure 3a) and AMF-corrected data (Figure 3b) diverge, likely due to increased uncertainties in trajectories and reduced/diluted SO$_2$ signal. Overall, the AMF-corrected SO$_2$ data appear to provide a more consistent and reasonable estimate of the total SO$_2$ loading of the plume; AMF correction similar to that discussed in section 3 is recommended for quantitative application of the operational OMI SO$_2$ product.

4.3. Change in the Aerosol Optical Depth Near the Plume Core

[21] Shown in Figure 3c is the average AOD near the plume core (rectangular box in Figure 2 on 5 April; various polygon boxes on 6 and 7 April). As the SO$_2$ mass decays with time, the average AOD near the main body of the plume increases. The polygon boxes on 6 and 7 April mainly cover the core part of the plume while the rectangular box on 5 April encircles both polluted and clean areas. This sampling difference can explain part of the AOD increase, but not all, as suggested by the rising AOD/SO$_2$ ratio in our sampling areas (~0.3 to ~0.5 DU^{-1} in the first two days). The average column SO$_2$ in two of the five polygon boxes on 6 April is actually greater than the plume-wide mean on 5 April, reflecting the sampling difference. At least part of the growth in AOD with time is likely caused by the introduction of outside aerosols and/or enhancement of aerosol extinction in the plume.

5. Discussion
5.1. Outside Contribution and Hygroscopic Growth of Aerosols

[22] Aerosols and SO$_2$ outside of the rectangular box on 5 April (initial plume area) might be carried into the polygon boxes on 6 and 7 April, contributing to the estimated SO$_2$ mass and average AOD in the boxes. The hygroscopic growth of aerosols may also enhance AOD. We conducted computational experiments to address these two factors. Forward trajectories similar to those described in section 2 are calculated over a larger area (30°N–49°N, 110°E–144°E). The hygroscopic growth effect on AOD is estimated with NCEP reanalysis RH along trajectories and various growth factors (α),

$$\frac{\text{AOD}_{\text{RH2}}}{\text{AOD}_{\text{RH1}}} = \left(\frac{1 - \text{RH1}}{1 - \text{RH2}}\right)^{-\alpha}, \qquad (14)$$

where RH1 and RH2 are the relative humidity at two different moments along a trajectory. Growth factor α when
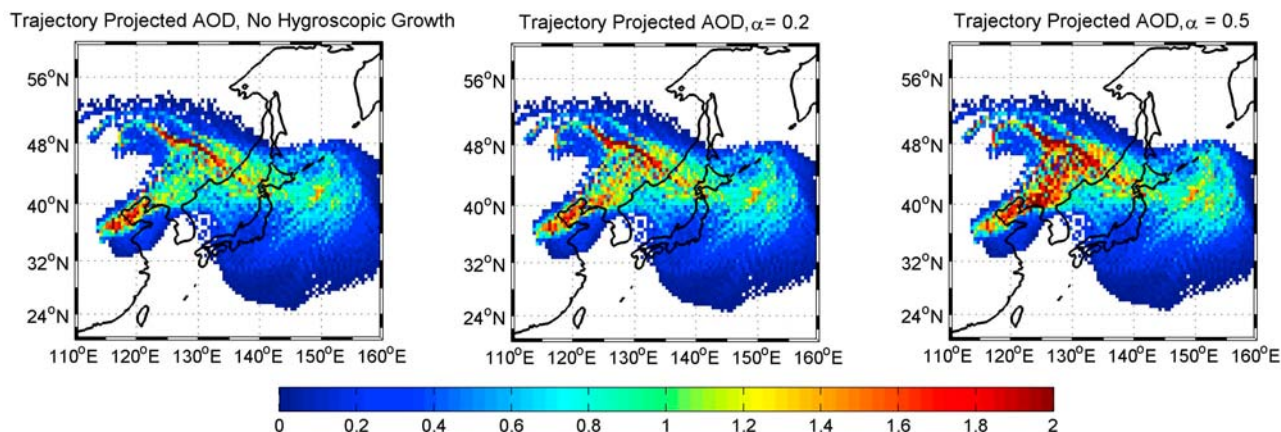
Figure 4. Trajectory-projected AOD on 6 April with contributions from outside of the initial plume area (rectangular box in Figure 2a) and aerosol hygroscopic growth accounted for. Hygroscopic growth is calculated with NCEP reanalysis RH along forward trajectories and values of α: (left) 0, (middle) 0.2, and (right) 0.5 (in equation (14)).

equal to zero represents aerosols with no hygroscopic growth; α of 0.5 corresponds to extremely hygroscopic aerosols. For reference, α is about 0.2–0.3 in summer months over the NE United States [*Taubman et al.*, 2004], where aerosols mainly consist of hygroscopic fine particles. Dust-dominated particles in this study are likely less hygroscopic. Figure 4 shows the trajectory-projected AOD on 6 April, with outside contribution and hygroscopic growth included (assumed α = 0, 0.2, and 0.5). Compared to Figure 2h, aerosols initially outside of the plume area can enhance AOD in polygon boxes on 6 April, particularly over the area east of Japan (around 40°N, 150°E, Figure 4). The effects of hygroscopic growth, in contrast, are relatively small except over the land W of the Sea of Japan. The trajectory-projected AOD including the outside contribution and aerosol swelling is compared to MODIS retrievals in Figure 5.

[23] To correct for the outside contribution to SO$_2$ mass, we first derive a different dispersion weighting factor, for example on 6 April for polygon $P1$,

$$\mathrm{DWF}_{P1,\mathrm{all}} = \frac{M_{P1,\mathrm{TRAJ,all}}}{M_1}, \tag{15}$$

where M_1 is the same as in equation (12), $M_{P1,\mathrm{TRAJ,all}}$ is the projected SO$_2$ mass using trajectories initiated from the larger area. Satellite determined SO$_2$ mass in $P1$ ($M_{P1,\mathrm{SAT}}$) is then weighted with the new DWF to estimate the total SO$_2$ mass on this day ($M_{2,P1,\mathrm{all}}$):

$$M_{2,P1,\mathrm{all}} = \frac{M_{P1,\mathrm{SAT}}}{\mathrm{DWF}_{P1,\mathrm{all}}}. \tag{16}$$

The assumption here is that SO$_2$ in the whole region (in and outside of the rectangular box in Figure 1a) decays at the same rate. The resulting total SO$_2$ mass of the plume ("SO$_2$ all," Figure 5a) is generally smaller than that without the correction ("SO$_2$ ini," Figure 5a), but the general decreasing trend in SO$_2$ remains largely unchanged.
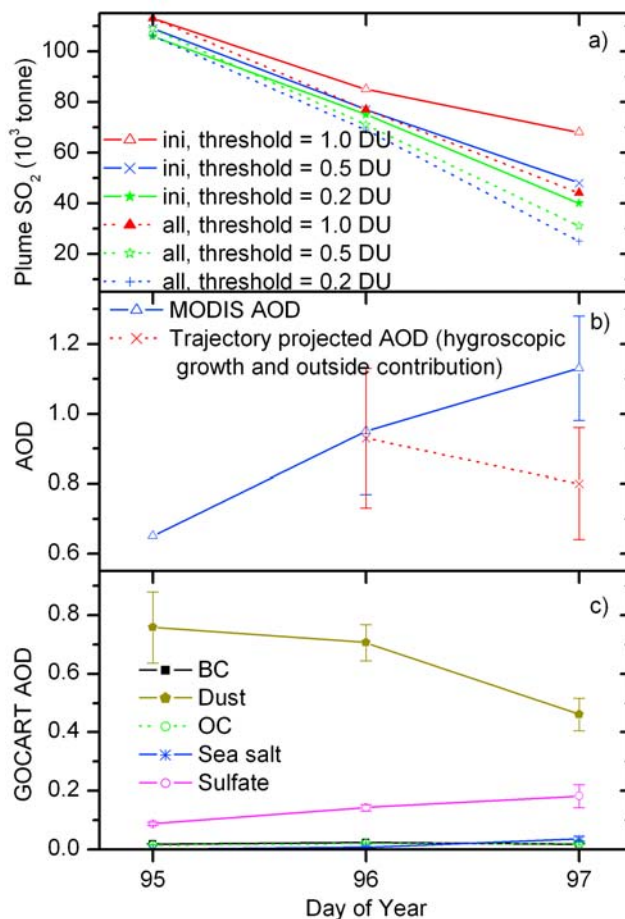
Figure 5. (a) Total SO$_2$ mass of the plume with (all) and without (ini) outside contribution corrected for. (b) MODIS and trajectory-projected average AOD including outside contribution and effects of hygroscopic growth near the core part of the plume. (c) AOD of different aerosol species near the main body of the plume in the output of GOCART model.
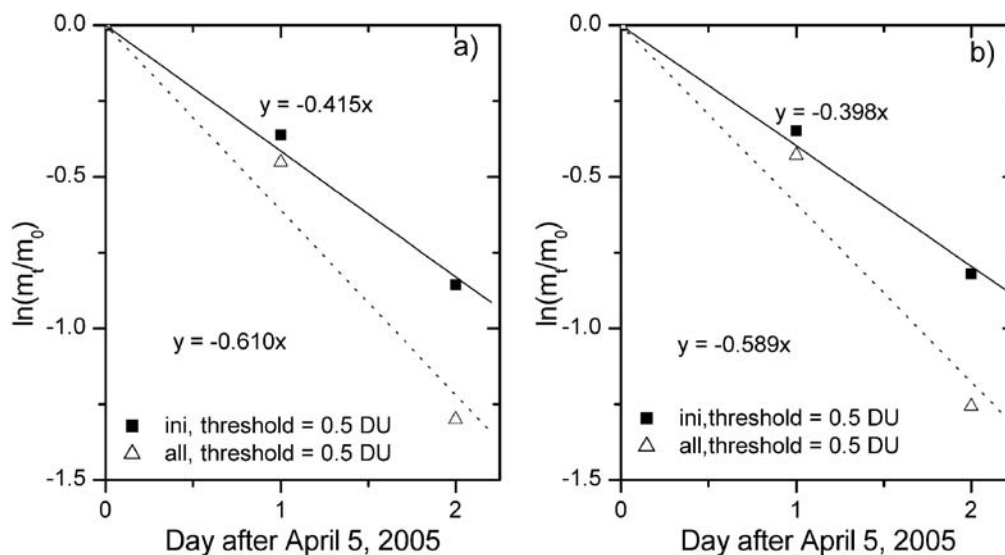
Figure 6. Decay plot of SO_2 in the plume from 5 to 7 April 2005 based on AMF-corrected SO_2 data (a) using GOCART aerosol composition and (b) assuming only dust particles. The slope of the linear fits in Figure 6a gives first-order removal rate of 0.42–0.61/d, which corresponds to SO_2 overall lifetime of 1.6–2.4 days. Linear fits in Figure 6b suggest SO_2 overall lifetime of 1.7–2.5 days. Decay plots of SO_2 loading with other threshold values give slightly different estimates of SO_2 lifetime (1.5–3.8 days assuming all dust for AMF correction; 1.4–3.5 days with GOCART aerosol composition for AMF correction).

5.2. Change in Aerosol Composition: Observations From Space and Model Simulations

[24] Supposing that all lost SO_2 converts to ammonium sulfate (assumed specific scattering coefficient: 4.2 m^2/g), the newly generated sulfate aerosols may add ∼0.1–0.2 to average AOD over the polygon boxes on 6 April, and ∼0.2–0.4 in AOD on 7 April. This is probably an over-estimate, since a fraction of SO_2 can be removed by dry deposition, and the interaction with dust may produce larger particles that scatter light less efficiently. Little difference is found between the observed and projected AOD on 6 April (Figure 5b); loss of dust from the plume probably cancels out the introduction of secondary aerosols. On 7 April, the difference between trajectory-projected and observed AOD is about 0.3. Current satellite instruments cannot discern different aerosol species, and we can sample the GOCART model output near the position of the plume on 5–7 April, at moments closest to satellite overpass. GOCART has a coarse horizontal resolution relative to satellite observations; the sampling domains for GOCART correspond roughly to the satellite sampling areas (rectangular and polygon boxes) in Figures 1 and 2, but are not exact matches. Qualitatively consistent with the satellite data, the GOCART simulation (Figure 5c) suggests that removal of dust and increase of sulfate are the most important processes controlling the change of aerosol loading in this plume. In this case study the generation of sulfate from SO_2 appears to be detectable from space, but the uncertainty is too high for quantitative estimates. Chemical transport models provide information about the aerosol chemical composition, and may help interpret the results.

[25] Clouds may contaminate MODIS AOD retrievals, and might produce more marked errors on 6 and 7 April, when cloud cover was greater. In a simple test we discard MODIS pixels with high AOD (>95th percentile) but small AE (<0.2) to remove possible cloud-contaminated data. This results in lower average AOD of 0.61, 0.88, and 1.03 on the 3 days, but does not change the overall trend of AOD. Adjusting the threshold of AOD and AE to filter out cloud-contaminated pixels gives slightly different but qualitatively consistent results.

5.3. Estimates of SO_2 Lifetime

[26] From the decay in SO_2 mass, we can approximate the overall SO_2 lifetime in this plume. Assuming first-order loss, the slope of the linear fit in Figure 6 gives the e-folding lifetime of SO_2. Our first estimate with operational SO_2 data and simple correction for plume dispersion was 3–5 days [*Dickerson et al.*, 2007]. With the aerosol composition information from GOCART, we can refine our assumption in AMF correction that dust is the only aerosol species (W = 1 in equation (10)) during the 3 day study period, by deriving the values of W based on GOCART simulated AOD of different species (W = 0.85, 0.79, 0.6 on 5, 6, and 7 April, respectively). The estimated SO_2 lifetime using the GOCART aerosol output is 1.4–3.5 days (Figure 6a), while the SO_2 lifetime estimated assuming W = 1 (only dust aerosols) is just slightly different at 1.5–3.8 days. In this dust-dominant case, the estimated SO_2 lifetime is relatively insensitive to the assumption about aerosol composition. Estimates based on both AMF corrections are in the range of prior modeling studies [*Berglen et al.*, 2004; *Chin et al.*, 2000; *Koch et al.*, 1999]. The calculated SO_2 mass on 7 April is far more diverse due to diluted signal. Excluding this day, the "best guess" SO_2 lifetime in this case is 2–3 days. If reaction with hydroxyl radical (OH) is the only SO_2 removal mechanism in this case, the derived SO_2 reaction rate requires OH concentration of ∼5 × 10^6 cm^{-3} (at ∼2000 m, temperature = 5°C [*Seinfeld and Pandis*, 1998]), which is much higher than normally expected for the altitude of this plume (∼1–3 km)

in springtime ($\sim$5 $\times$ 10^5 molecules/cm^3 in January, $\sim$3 $\times$ 10^6 molecules/cm^3 in July [*Chin et al.*, 2000]). Thus dry deposition and in-cloud processing or other oxidation processes probably account for at least part of the observed SO_2 loss.

6. Conclusions

[27] In this paper we use satellite data to further study the long-range transport of a regional pollution plume, first observed over NE China on 5 April 2005 during the EAST-AIRE aircraft campaign [*Dickerson et al.*, 2007; *Krotkov et al.*, 2008]. OMI and MODIS, two sensors of the A-train satellite constellation show that the plume with substantial SO_2 ($\sim$110,000 tonne) and high loadings of dust particles covered a large region over East Asia (mainly China). Based on a forward trajectory tracer model, this large SO_2 dust plume migrated eastward with the weather system, passed over northern Japan on 6 April, and traveled over the NW Pacific on 7 April. Satellites, in agreement with the forward trajectory modeling, successfully capture the plume from space along its transport pathway on a daily basis. The good agreement between satellite data and the trajectory model, particularly that between the OMI aerosol index and model-projected aerosol plume, suggests that OMI can be a useful tool studying episodic long-range transport events.

[28] The fresh plume over the source area has high SO_2 loading that can be readily detected by OMI. Several factors can change the SO_2 signal as the plume moves downwind: dispersion of the plume, chemical reaction, and dry deposition of SO_2 can reduce the signal; lofting of the plume (change of SO_2 vertical distribution) can enhance the signal; clouds can add to the OMI sensitivity to SO_2 above them but block SO_2 beneath. The overall result for this case, and very likely for other transport events in the lower troposphere, is that part of the SO_2 plume that can be detected over the source region would become less visible to OMI over downwind areas. Thus it is difficult to quantify the change of the total SO_2 mass within the plume during transport, with OMI retrievals alone. In this study, we demonstrate a method that combines the strengths of trajectory tracer model and OMI retrievals: the trajectory model projects the position of the plume core; OMI measures the SO_2 mass within the plume core; the trajectory model estimates the rest of the plume assuming the same rate of SO_2 loss as in the plume core. AMF correction made in this study accounts for effects of SO_2 profile, aerosols, clouds, and satellite viewing geometry on retrievals. The estimated SO_2 mass of the plume based on the AMF-corrected SO_2 data is more consistent, compared to that from the operational SO_2 product. In short, for any quantitative application of the OMI SO_2 data in studies on pollution transport, AMF corrections and trajectory tracer modeling are recommended.

[29] The overall lifetime SO_2 (e-folding time) estimated with our method, derived from the decay of the SO_2 loading of the plume assuming first-order loss, is 1.5–3.8 days, and in line with previous estimates but faster than can be accounted for by OH reaction alone. For this particular dust-dominant case, the derived lifetime is insensitive to the assumptions concerning aerosol composition. Using the aerosol composition information from the GOCART model for AMF correction (instead of all dust assumed in our cal-

culation), the estimated SO_2 lifetime changes only slightly to 1.4–3.5 days. For other cases, aerosol composition information can be more important.

[30] Assuming all lost SO_2 becomes to ammonium sulfate during transport, this process can generate an AOD signal up to a few tenths near the plume core, strong enough to be detected from space. The satellite retrieved average AOD near the core part of the plume is close to the trajectory-projected value (hygroscopic growth and outside contribution accounted for, but no loss of primary aerosols) over northern Japan on 6 April; to this point the introduction of secondary aerosols and the loss of primary aerosols (dust) may have canceled out. MODIS AOD is greater than the trajectory AOD over NW Pacific on 7 April. The GOCART model demonstrates that dust AOD decreases while sulfate AOD grows as the plume moves away from its source region in northern China. Satellites appear to be able to detect the formation of secondary aerosols in this episode, but the results are qualitative, and chemical transport models can be used to make the results more quantitative.

[31] In summary, in this case study we are able to improve our quantification of pollutant concentration change during a transport event using satellite data. Trajectory tracer modeling and AMF correction of OMI SO_2 data are important parts of the method proposed in this study, and are recommend for future, quantitative use of OMI SO_2 data. Satellites can potentially detect the conversion from primary gases to secondary aerosols in long-range transport events, although more work is needed to reduce the uncertainties. The method can be applied to other data sources (satellite sensors) and cases, and further developed to investigate the transport and evolution of pollution plumes and their interactions with weather and climate.

References

Ahmad, Z., P. K. Bhartia, and N. Krotkov (2004), Spectral properties of backscattered UV radiation in cloudy atmospheres, *J. Geophys. Res.*, *109*, D01201, doi:10.1029/2003JD003395.

Akimoto, H., T. Ohara, J. Kurokawa, and N. Horii (2006), Verification of energy consumption in China during 1996–2003 by using satellite observational data, *Atmos. Environ.*, *40*, 7663–7667, doi:10.1016/j.atmosenv.2006.07.052.

Allen, D., K. Pickering, and M. Fox-Rabinovitz (2004), Evaluation of pollutant outflow and CO sources during TRACE-P using model-calculated, aircraft-based, and Measurements of Pollution in the Troposphere (MOPITT)-derived CO concentrations, *J. Geophys. Res.*, *109*, D15S03, doi:10.1029/2003JD004250.

Anderson, T. L., et al. (2005), An "A-Train" strategy for quantifying direct climate forcing by anthropogenic aerosols, *Bull. Am. Meteorol. Soc.*, *86*(12), 1795–1809, doi:10.1175/BAMS-86-12-1795.

Baumgardner, D., R. Subramanian, C. Twohy, J. Stith, and G. Kok (2008), Scavenging of black carbon by ice crystals over the northern Pacific, *Geophys. Res. Lett.*, *35*, L22815, doi:10.1029/2008GL035764.

Berglen, T. F., T. K. Berntsen, I. S. A. Isaksen, and J. K. Sundet (2004), A global model of the coupled sulfur/oxidant chemistry in the troposphere: The sulfur cycle, *J. Geophys. Res.*, *109*, D19310, doi:10.1029/2003JD003948.

Carmichael, G. R., et al. (2003), Evaluating regional emission estimates using the TRACE-P observations, *J. Geophys. Res.*, *108*(D21), 8810, doi:10.1029/2002JD003116.

Chin, M., D. Savoie, B. Huebert, A. Bandy, D. Thornton, T. Bates, P. Quinn, E. Saltzman, and W. De Bruyn (2000), Atmospheric sulfur cycle simulated in the global model GOCART: Comparison with field observations and regional budgets, *J. Geophys. Res.*, *105*(D20), 24,689–24,712, doi:10.1029/2000JD900385.

Chin, M., P. Ginoux, S. Kinne, O. Torres, B. N. Holben, B. N. Duncan, R. V. Martin, J. A. Logan, A. Higurashi, and T. Nakajima (2002), Tropospheric aerosol optical thickness from the GOCART model and comparisons with satellite and Sun photometer measurements, *J. Atmos. Sci.*, *59*, 461–483, doi:10.1175/1520-0469(2002)059<0461:TAOTFT>2.0.CO;2.

Dickerson, R. R., et al. (2007), Aircraft observations of dust and pollutants over NE China: Insight into the meteorological mechanisms of long-range transport, *J. Geophys. Res.*, *112*, D24S90, doi:10.1029/2007JD008999.

Engel-Cox, J. A., C. H. Holloman, B. W. Coutant, and R. M. Hoff (2004), Qualitative and quantitative evaluation of MODIS satellite sensor data for regional and urban scale air quality, *Atmos. Environ.*, *38*, 2495–2509, doi:10.1016/j.atmosenv.2004.01.039.

Fairlie, T. D., D. J. Jacob, and R. J. Park (2007), The impact of transpacific transport of mineral dust in the United States, *Atmos. Environ.*, *41*, 1251–1266.

Fuelberg, H. E., C. M. Kiley, J. R. Hannan, D. J. Westberg, M. A. Avery, and R. E. Newell (2003), Meteorological conditions and transport pathways during the Transport and Chemical Evolution over the Pacific (TRACE-P) experiment, *J. Geophys. Res.*, *108*(D20), 8782, doi:10.1029/2002JD003092.

Ginoux, P., M. Chin, I. Tegen, J. Prospero, B. Holben, O. Dubovik, and S.-J. Lin (2001), Sources and distributions of dust aerosols simulated with the GOCART model, *J. Geophys. Res.*, *106*(D17), 20,255–20,273, doi:10.1029/2000JD000053.

Huang, J., P. Minnis, B. Chen, Z. Huang, Z. Liu, Q. Zhao, Y. Yi, and J. K. Ayers (2008), Long-range transport and vertical structure of Asian dust from CALIPSO and surface measurements during PACDEX, *J. Geophys. Res.*, *113*, D23212, doi:10.1029/2008JD010620.

Husar, R. B., et al. (2001), Asian dust events of April 1998, *J. Geophys. Res.*, *106*(D16), 18,317–18,330, doi:10.1029/2000JD900788.

Intergovernmental Panel on Climate Change (2001), *Climate Change 2001: The Scientific Basis*, 881 pp., Cambridge Univ. Press, Cambridge, U. K.

Jacob, D. J., J. H. Crawford, M. M. Kleb, V. S. Connors, R. J. Bendura, J. L. Raper, G. W. Sachse, J. C. Gille, L. Emmons, and C. L. Heald (2003), Transport and Chemical Evolution over the Pacific (TRACE-P) aircraft mission: Design, execution, and first results, *J. Geophys. Res.*, *108*(D20), 9000, doi:10.1029/2002JD003276.

Jaffe, D. A., et al. (1999), Transport of Asian air pollution to North America, *Geophys. Res. Lett.*, *26*, 711–714, doi:10.1029/1999GL900100.

Jaffe, D. A., I. McKendry, T. Anderson, and H. Price (2003a), Six 'new' episodes of trans-Pacific transport of air pollutants, *Atmos. Environ.*, *37*, 391–404, doi:10.1016/S1352-2310(02)00862-2.

Jaffe, D. A., D. Parrish, A. Goldstein, H. Price, and J. Harris (2003b), Increasing background ozone during spring on the west coast of North America, *Geophys. Res. Lett.*, *30*(12), 1613, doi:10.1029/2003GL017024.

Koch, D., D. Jacob, I. Tegen, D. Rind, and M. Chin (1999), Tropospheric sulfur simulation and sulfate direct radiative forcing in the Goddard Institute for Space Studies general circulation model, *J. Geophys. Res.*, *104*(D19), 23,799–23,822, doi:10.1029/1999JD900248.

Krotkov, N. A., et al. (2006), Band residual difference algorithm for retrieval of SO_2 from the Aura Ozone Monitoring Instrument (OMI), *IEEE Trans. Geosci. Remote Sens.*, *44*, 1259–1266, doi:10.1109/TGRS.2005.861932.

Krotkov, N. A., et al. (2008), Validation of SO_2 retrievals from the Ozone Monitoring Instrument over NE China, *J. Geophys. Res.*, *113*, D16S40, doi:10.1029/2007JD008818.

Levy, R. C., L. A. Remer, S. Mattoo, E. Vermote, and Y. J. Kaufman (2007a), Second-generation operational algorithm: Retrieval of aerosol properties over land from inversion of Moderate Resolution Imaging Spectroradiometer spectral reflectance, *J. Geophys. Res.*, *112*, D13211, doi:10.1029/2006JD007811.

Levy, R. C., L. A. Remer, and O. Dubovic (2007b), Global aerosol optical models and application to MODIS aerosol retrieval over land, *J. Geophys. Res.*, *112*, D13210, doi:10.1029/2006JD007815.

Li, C. (2008), Emissions, transport, and evolution of atmospheric pollutants from China: An observational study, Ph.D. dissertation, 221 pp., Univ. of Md., College Park.

Li, C., L. T. Marufu, R. R. Dickerson, Z. Li, T. Wen, Y. Wang, P. Wang, H. Chen, and J. W. Stehr (2007), In situ measurements of trace gases and aerosol optical properties at a rural site in northern China during East Asian Study of Tropospheric Aerosols: An International Regional Experiment 2005, *J. Geophys. Res.*, *112*, D22S04, doi:10.1029/2006JD007592.

Li, Z., et al. (2007a), Preface to special section on East Asian Studies of Tropospheric Aerosols: An International Regional Experiment (EAST-AIRE), *J. Geophys. Res.*, *112*, D22S00, doi:10.1029/2007JD008853.

Li, Z., F. Niu, K.-H. Lee, J. Xin, W.-M. Hao, B. Nordgren, Y. Wang, and P. Wang (2007b), Validation and understanding of Moderate Resolution Imaging Spectroradiometer aerosol products (C5) using ground-based measurements from the handheld Sun photometer network in China, *J. Geophys. Res.*, *112*, D22S07, doi:10.1029/2007JD008479.

Liu, J., J. R. Drummond, D. B. A. Jones, Z. Cao, H. Bremer, J. Kar, J. Zou, F. Nichitiu, and J. C. Gille (2006), Large horizontal gradients in atmospheric CO at the synoptic scale as seen by spaceborne Measurements of Pollution in the Troposphere, *J. Geophys. Res.*, *111*, D02306, doi:10.1029/2005JD006076.

Martin, R. V. (2008), Satellite remote sensing of surface air quality, *Atmos. Environ.*, *42*, 7823–7843, doi:10.1016/j.atmosenv.2008.07.018.

Menzal, W. P., R. A. Frey, B. A. Baum, and H. Zhang (2006), Cloud top properties and cloud phase algorithm theoretic basis document, *MOD06CT/MYD06CT ATBD C005*, 55 pp., NASA Goddard Space Flight Cent., Greenbelt, Md.

Methven, J., et al. (2006), Establishing Lagrangian connections between observations within air masses crossing the Atlantic during the International Consortium for Atmospheric Research on Transport and Transformation experiment, *J. Geophys. Res.*, *111*, D23S62, doi:10.1029/2006JD007540.

Mi, W., Z. Li, X. Xia, B. Holben, R. Levy, F. Zhao, H. Chen, and M. Cribb (2007), Evaluation of MODIS aerosol products at two AERONET stations in China, *J. Geophys. Res.*, *112*, D22S08, doi:10.1029/2007JD008474.

Remer, L. A., et al. (2005), The MODIS aerosol algorithm, products and validation, *J. Atmos. Sci.*, *62*, 947–973, doi:10.1175/JAS3385.1.

Richter, A., J. P. Burrows, H. Nüß, C. Granier, and U. Niemeier (2005), Increase in tropospheric nitrogen dioxide over China observed from space, *Nature*, *437*, 129–132, doi:10.1038/nature04092.

Seinfeld, J. H., and S. N. Pandis (1998), *Atmospheric Chemistry and Physics: From Air Pollution to Climate Change*, 1326 pp., John Wiley, Hoboken, N. J.

Shimizu, A., N. Sugimoto, I. Matsui, K. Arao, I. Uno, T. Murayama, N. Kagawa, K. Aoki, A. Uchiyama, and A. Yamazaki (2004), Continuous observations of Asian dust and other aerosols by polarization lidars in China and Japan during ACE-Asia, *J. Geophys. Res.*, *109*, D19S17, doi:10.1029/2002JD003253.

Stohl, A., C. Forster, S. Eckhardt, N. Spichtinger, H. Huntrieser, J. Heland, H. Schlager, S. Wilhelm, F. Arnold, and O. Cooper (2003), A backward modeling study of intercontinental pollution transport using aircraft measurements, *J. Geophys. Res.*, *108*(D12), 4370, doi:10.1029/2002JD002862.

Taubman, B. F., L. Marufu, B. Vant-Hull, C. Piety, B. Doddridge, R. Dickerson, and Z. Li (2004), Smoke over haze: Aircraft observations of chemical and optical properties and the effects on heating rates and stability, *J. Geophys. Res.*, *109*, D02206, doi:10.1029/2003JD003898.

Taubman, B. F., J. C. Hains, L. T. Marufu, B. G. Doddridge, A. M. Thompson, J. W. Stehr, C. A. Piety, and R. R. Dickerson (2006), Aircraft vertical profiles of trace gas and aerosol pollution over the mid-Atlantic United States: Statistics and meteorological cluster analysis, *J. Geophys. Res.*, *111*, D10S07, doi:10.1029/2005JD006196.

van Donkelaar, A., et al. (2008), Analysis of aircraft and satellite measurements from the Intercontinental Chemical Transport Experiment (INTEX-B) to quantify long-range transport of East Asian sulfur to Canada, *Atmos. Chem. Phys.*, *8*, 2991–3014.

Wang, Y., M. B. McElroy, K. F. Boersma, H. J. Eskes, and J. P. Veefkind (2007), Traffic restrictions associated with the Sino-African summit: Reductions of NO_x detected from space, *Geophys. Res. Lett.*, *34*, L08814, doi:10.1029/2007GL029326.

Zhang, R., G. Li, J. Fan, D. L. Wu, and M. J. Molina (2007), Intensification of Pacific storm track linked to Asian pollution, *Proc. Natl. Acad. Sci. U. S. A.*, *104*, 5295–5299, doi:10.1073/pnas.0700618104.

————————

M. Chin, NASA Goddard Space Flight Center, Greenbelt, MD 20771, USA.

R. R. Dickerson, C. Li, and Z. Li, Department of Atmospheric and Oceanic Science, University of Maryland, College Park, MD 20742, USA. (can.li@nasa.gov)

N. A. Krotkov and K. Yang, Goddard Earth Sciences and Technology Center, University of Maryland Baltimore County, Baltimore, MD 21250, USA.